

Tracking Position and Orientation of Magnetic Objects Using Magnetometer Networks

Niklas Wahlström and Fredrik Gustafsson

Linköping University Post Print



Copyright: The Authors

Preprint ahead of publication available at: Linköping University Electronic Press
<http://urn.kb.se/resolve?urn=urn:nbn:se:liu:diva-122395>

Tracking Position and Orientation of Magnetic Objects using Magnetometer Networks

Niklas Wahlström, *Student Member, IEEE*, Fredrik Gustafsson, *Fellow, IEEE*,

Abstract—A framework for estimation and filtering of magnetic dipoles in a network of magnetometers is presented. The application in mind is tracking of objects consisting of permanent magnets for controlling computer applications, though the framework can also be applied to tracking larger objects such as vehicles. A general sensor model for the network is presented for tracking objects consisting of (i) a single dipole, (ii) a structure of dipoles and (iii) several freely moving (structures of) dipoles, respectively. A single dipole generates a magnetic field with rotation symmetry, so at best five degrees of freedom (5D) tracking can be achieved, where the SNR decays cubically with distance. One contribution is the use of structures of dipoles, which allows for full 6D tracking if the dipole structure is large enough. An observability analysis shows that the sixth degree of freedom is weakly observable, where the SNR decays to the power of four with distance, and that there is a 180 degree ambiguity around a specific symmetry axis. Experimental results are presented and compared to a reference tracking system, and four public demonstrators based on this framework are briefly described.

Index Terms—Magnetic dipole, Kalman filtering, sensor networks

I. INTRODUCTION

Magnetic localization offers many advantages in comparison to other localization techniques in terms accuracy, robustness, and cost. The technique has for the last decade primarily been used in applications to track medical apparatus inside the human body [1], [2], [3], in traffic surveillance to detect and localize ground and maritime vehicles [4], [5], [6], and more lately in in computer gaming industry [7], [8], [9], [10]. Magnetic localization can provide accurate position and orientation estimates in applications for which occlusion disqualifies vision sensors, and lack of absolute position excludes pure IMU-based approaches. Further the magnetic field does not suffer from multi-path and scattering effects as in radio-based solutions.

This paper considers a sensor network of vector magnetometers that is used to determine the position and orientation of a permanently magnetized object, for example a magnet. We suggest a filtering framework including measurement and motion models that can be used to determine both the position and the orientation of the magnet based on the magnetometer measurements. We also present a range of applications in which this technique have been successfully implemented. This extends the palette of applications mentioned above. These applications have been realized with low-graded magnetometers (a few dollars each) that can be found in standard smartphones.

The use of stationary magnetometers to determine position and orientation is proposed in several publications [11], [12], [13], [14]. They model the object as a magnetic dipole moment inducing a magnetic dipole field that can be computed analytically. This magnetic dipole moment includes both position and orientation of that object as well as its magnetic strength. This initial work has been further elaborated by Yabukami et al. [15], [16], Hu et al [17], [18], [19], [20] and researchers at Institute of Physiology, University of Lausanne [1], [2]. Their primary application has been to record images of the digestive track, so-called capsule endoscopy, where a capsule equipped with a small magnet can be localized during its path through the tract. All of these contributions have in common that they compute the position and orientation of the object at each time instant separately (typically using Levenberg-Marquardt algorithm). Sherman et al. [21] demonstrate that these tracking systems manage to obtain a precision of 1 mm for position and 1° in orientation within a range of 100 mm, in that case using a network of 27 scalar magnetometers.

Birsan [22], [4] and Kozick and Sadler [5], [23], [24] have used magnetometers to localize ground vehicles, the latter also fusing magnetometers with acoustic sensors.

This contribution presents a general framework for tracking one or several magnetic objects using a sensor network of magnetometers, extending the theory in the aforementioned references in several aspects:

- 1) A general sensor model that relates an object including at least one magnetic dipole and a general network of magnetometers, where the model also includes calibration parameters. Specific models for objects consisting of a single dipole (enabling 5D pose estimation), a structure of dipoles (for 6D pose), and several separate (structures of) dipoles (allowing multiple objects to be tracked). This is presented in Section II. Together with these sensor models, different orientation representations are considered. They are described in Section III.
- 2) The use of objects that consist of structures of dipoles is supposedly an original contribution. Therefore, an observability analysis is presented, based on a Taylor expansion of the sensor model. The first term shows the intuitive result that if the object is far away from the sensor network, the structure will appear as one single dipole, and the orientation around the symmetry axis of a dipole equivalent will be lost. By a proper definition of the origin of the object, the symmetry axis can be defined easily. The second order Taylor term shows an interesting result in that that the sensor model is bimodal. A 180° flip of the object around the symmetry axis will give the same Taylor term. This analysis is presented in

Section IV with additional material in Appendix A.

- 3) A couple of motion models for temporal filtering. These models explore different ways to parametrize the orientation, suitable for tracking pose in 5D and 6D, respectively. These motion models are described in Section V.
- 4) Section VI presents performance results when tracking a single and double dipole, respectively, compared to a reference tracking system. Section VII briefly describes four applications based on the filtering framework presented in this paper.

II. SENSOR MODEL

In a statistical signal processing framework, measurements can be described with a stochastic state-space model

$$\mathbf{x}_{k+1} = F_k \mathbf{x}_k + G_k \mathbf{w}_k, \quad \mathbf{w}_k \sim \mathcal{N}(\mathbf{0}, Q), \quad (1a)$$

$$\mathbf{y}_k = \mathbf{h}(\mathbf{x}_k) + \mathbf{e}_k, \quad \mathbf{e}_k \sim \mathcal{N}(\mathbf{0}, R), \quad (1b)$$

where \mathbf{y}_k is the measurement, \mathbf{x}_k is the state of the system, \mathbf{w}_k is the process noise and \mathbf{e}_k is the measurement noise, all at time instant kT , T being the sample period. The process and measurement noises are assumed to be white Gaussian with $\mathbf{w}_k \sim \mathcal{N}(\mathbf{0}, Q)$ and $\mathbf{e}_k \sim \mathcal{N}(\mathbf{0}, R)$. The motion model (1a) is explained in Section V and the sensor model (1b) is described in this section.

The measurement from a stationary vector-magnetometer $\tilde{\mathbf{y}}_k$ can be decomposed into a constant bias term \mathbf{B}_0 and a time varying term $\mathbf{h}(\mathbf{x}_k)$, where

$$\tilde{\mathbf{y}}_k = \mathbf{B}_0 + \mathbf{h}(\mathbf{x}_k) + \mathbf{e}_k. \quad (2)$$

The constant bias term is in turn composed of the earth magnetic field, magnetic distortions due the stationary magnetic environment, and sensor biases. This bias term can be measured during a calibration phase before any magnetic object enters the scene to then be subtracted from the measurements. This approach is advocated in this paper and we therefore only consider the calibrated measurement $\mathbf{y}_k = \tilde{\mathbf{y}}_k - \mathbf{B}_0$ onwards. Optionally, the bias could also be estimated jointly with the state \mathbf{x}_k as a part of the filtering.

In this work, the time varying term represents magnetic distortions from moving objects that consist of permanent magnets. These objects are modeled with magnetic dipoles, where each dipole corresponds to a magnet. We present a single dipole model in Section II-A, continue by extending this to a multi-dipole model in Section II-B, and finally a multi-object model in Section II-C. In the model description, two coordinates systems are considered; (i) the global coordinate system, which is the coordinate system of the stationary sensor network, and (ii) the local coordinate system, which is the body-fixed coordinate system of the moving object. For the quantities that are presented in this paper, \mathbf{s}_l , \mathbf{b}_l and U are defined in local coordinates, whereas \mathbf{y}_k , \mathbf{r}_k , \mathbf{m}_k , \mathbf{q}_k , R_k , $\boldsymbol{\theta}_j$, \mathbf{v}_k , $\boldsymbol{\omega}_k$ and \mathbf{W}_k are given in global coordinates.

A. Single Dipole Model

A magnetic dipole produces a magnetic dipole field that can be derived from Maxwell's equations. This field decays cubically with the distance to the dipole. With J magnetometers

positioned at $\{\boldsymbol{\theta}_j\}_{j=1}^J$, we obtain the following sensor model for the j th sensor

$$\mathbf{h}_j(\mathbf{x}_k) = J(\mathbf{r}_k - \boldsymbol{\theta}_j) \mathbf{m}_k, \quad (3)$$

$$J(\mathbf{r}) = \frac{1}{\|\mathbf{r}\|^5} (3\mathbf{r}\mathbf{r}^T - \|\mathbf{r}\|^2 I_3), \quad (4)$$

where \mathbf{m}_k is the magnetic dipole moment of the magnet, $\mathbf{r}_k = [r_k^{(x)}, r_k^{(y)}, r_k^{(z)}]$ is the position in Cartesian coordinates, both given in global coordinates, and \mathbf{x}_k is the state of the system.

The magnetic dipole moment $\mathbf{m}_k \in \mathbb{R}^3$ has both a magnitude and a direction. The magnetic field produced is proportional to the magnitude $m = \|\mathbf{m}_k\|$ and the orientation of the object is represented by the direction of \mathbf{m}_k . In the single dipole model, we use \mathbf{m}_k as a part of the state vector \mathbf{x}_k to encode both the orientation and the strength of the magnet.

Note that this orientation representation only encodes two degrees of freedom (DoF) for the orientation. In fact, only two DoF are observable in (3) because the dipole field is symmetric around \mathbf{m}_k . By applying an additional rotation around the dipole moment \mathbf{m}_k , its direction does not change.

B. Multi-Dipole Model

The symmetry present in the single dipole model can be broken by considering objects with multiple dipoles. Therefore, to obtain all three DoF for the orientation, a multi-dipole object is considered. It consists of L magnetic dipole moments with a predefined and constant geometry. Since magnetic fields from multiple sources superpose, the sensor model is constructed by adding multiple dipole fields.

Consider the l th dipole moment to be located at position \mathbf{s}_l relative to the center of the object with the direction \mathbf{b}_l , where $\|\mathbf{b}_l\| = 1$. Both \mathbf{s}_l and \mathbf{b}_l are provided in local coordinates. See Figure 1 for an example of such a geometry including two dipoles.

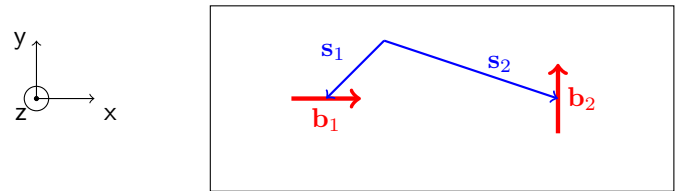


Fig. 1: The geometry of a multi-dipole object with two dipoles. The vectors \mathbf{s}_1 and \mathbf{s}_2 describe the position of the two dipole moments, and the vectors \mathbf{b}_1 and \mathbf{b}_2 their directions. The two magnets are in this example aligned perpendicular to each other with the first dipole pointing towards the second dipole. This geometry also illustrates the setup that was used in the experiment in Section VI-B.

Each magnetic dipole moment $\mathbf{m}_{k,l}$ can then be expressed with its direction \mathbf{b}_l , its unknown magnitude m_l , and a rotation matrix R_k that relates the orientation of the object relative to the global coordinate frame

$$\mathbf{m}_{k,l} = m_l R_k \mathbf{b}_l. \quad (5)$$

Further, the position of dipole l is given by $\mathbf{r}_k + R_k \mathbf{s}_l$, where $R_k \mathbf{s}_l$ is the displacement of dipole l in global coordinates

relative to the center of the object. With all combined, the sensor model is given by

$$\mathbf{h}_j(\mathbf{x}_k) = \sum_{l=1}^L J(\mathbf{r}_k + R_k \mathbf{s}_l - \boldsymbol{\theta}_j) m_l R_k \mathbf{b}_l, \quad (6)$$

where \mathbf{r}_k , R_k and $\{m_l\}_{l=1:L}$ are the unknown components. The parametrization of R_k is further discussed in Section III.

C. Multi-Object Multi-Dipole Model

The multi-dipole model can be further extended to a model for multiple multi-dipole objects. As discussed above, the contributions from all objects superpose and the corresponding sensor model is given by

$$\mathbf{h}_j(\mathbf{x}_k) = \sum_{i=1}^M \sum_{l=1}^L J(\mathbf{r}_{k,i} + R_{k,i} \mathbf{s}_l - \boldsymbol{\theta}_j) m_{l,i} R_{k,i} \mathbf{b}_{l,i}, \quad (7)$$

where $\mathbf{r}_{k,i}$ and $R_{k,i}$ describe the position and the orientation of i th object, respectively.

Note that neither more objects nor extended objects do result in an increased number of measurements as otherwise common in multiple and extended target tracking [25]. The number of measurements depend on the number of sensors deployed and not on the number of objects present in the scene. This makes it significantly more difficult to track multiple objects in comparison to a single object. For this reason, we only present experimental results for the single dipole model (3) and the multi-dipole model (6) in Section VI. The multi-object model is included to provide a general framework.

III. ORIENTATION REPRESENTATIONS

Whereas the position is parametrized with a three-dimensional Cartesian vector throughout this paper, different parametrizations for the orientation are considered. In this section, three different orientation representations are introduced and compared.

A. Magnetic Dipole Moment

In the single dipole model (3), the magnetic dipole moment \mathbf{m}_k encodes both the orientation and the magnitude of the dipole. This can be described with a rotation matrix R_k giving

$$\mathbf{m}_k = m R_k \mathbf{b}, \quad (8)$$

where \mathbf{b} , with $\|\mathbf{b}\| = 1$, denotes the direction of the dipole in local coordinates.

As already discussed, this orientation representation only encodes two degrees of freedom (DoF) for the orientation. In the control literature, similar applications are referred to as pointing applications [26]. In that context, a reduced representation of the rotation matrix can be expressed using the reduced-attitude vector $\boldsymbol{\gamma}_k = R_k \mathbf{b}$. In our context, $\boldsymbol{\gamma}_k$, with $\|\boldsymbol{\gamma}_k\| = 1$, describes the direction of the magnetic dipole vector in global coordinates and the magnetic dipole moment is expressed as

$$\mathbf{m}_k = m \cdot \boldsymbol{\gamma}_k. \quad (9)$$

Instead of using separate parameters for m and $\boldsymbol{\gamma}_k$, they can be combined into one “extended” reduced-attitude vector $\bar{\boldsymbol{\gamma}}_k = m \cdot \boldsymbol{\gamma}_k \in \mathbb{R}^3$. This parametrization is obviously equivalent of using the parameters in the magnetic dipole vector itself

$$\mathbf{m}_k = \bar{\boldsymbol{\gamma}}_k. \quad (10)$$

The assumption that $\|\mathbf{m}_k\|$ shall remain constant can be incorporated in the dynamical model, see Section V-B.

B. Unit Quaternion

In (5), a rotation matrix was used to describe the full orientation state of the object. Since all three DoF are needed, the approach discussed in the Section III-A does not work. We instead use quaternions.

Unit quaternions $\mathbf{q} \in \mathbb{R}^4$, with $\|\mathbf{q}\| = 1$, are popular for parametrizing rotation matrices, see for example [27]. This parametrization avoids singularities otherwise present while using Euler angles. The rotation matrix is given by $R_k = R(\mathbf{q}_k)$, where the elements of $R(\mathbf{q}_k)$ are quadratic expression in the elements of $\mathbf{q} = [q_0 \ q_1 \ q_2 \ q_3]^T$, where

$$R(\mathbf{q}) = \begin{bmatrix} q_0^2 + q_1^2 - q_2^2 - q_3^2 & 2q_1q_2 - 2q_0q_3 & 2q_1q_3 + 2q_0q_2 \\ 2q_1q_2 + 2q_0q_3 & q_0^2 - q_1^2 + q_2^2 - q_3^2 & 2q_2q_3 - 2q_0q_1 \\ 2q_1q_3 - 2q_0q_2 & 2q_2q_3 + 2q_0q_1 & q_0^2 - q_1^2 - q_2^2 + q_3^2 \end{bmatrix}. \quad (11)$$

The sensor model is then given by (6) with $R_k = R(\mathbf{q}_k)$, where \mathbf{r}_k , \mathbf{q}_k , and $\{m_l\}_{l=1:L}$ are contained in the state \mathbf{x}_k .

C. Extended Quaternion

By further assuming that all magnetic dipoles have the same unknown magnitude m , a compact representation of \mathbf{q}_k and m can be achieved. This assumption can be relaxed by assuming that the relative magnitudes of the dipoles are known. These relative magnitudes can then be encoded in the magnitudes of \mathbf{b} . Note that this assumption is not too restrictive since magnets of use are normally of the same kind. Their relative magnitudes can be measured based on their relative size (or weight), or assumed to have the same magnitude if they are identical.

With this assumption, (5) can, in a similar manner as for the extended reduced-attitude vector described in Section III-A, be rewritten as

$$\mathbf{m}_{k,l} = R(\bar{\mathbf{q}}_k) \mathbf{b}_l, \quad \text{where } \bar{\mathbf{q}}_k = \sqrt{m} \mathbf{q}_k. \quad (12)$$

This defines an extended quaternion $\bar{\mathbf{q}}_k$ that not only encodes the orientation of the object, but also the magnitude of the magnetic dipoles. This combined with the sensor model (6) gives

$$\mathbf{h}_j(\mathbf{x}_k) = \sum_{l=1}^L J(\mathbf{r}_k + R_k \mathbf{s}_l - \boldsymbol{\theta}_j) \mathbf{m}_{k,l}, \quad (13a)$$

$$\text{where } R_k = R\left(\frac{\bar{\mathbf{q}}_k}{\|\bar{\mathbf{q}}_k\|}\right), \quad \mathbf{m}_{k,l} = R(\bar{\mathbf{q}}_k) \mathbf{b}_l, \quad (13b)$$

where \mathbf{r}_k and $\bar{\mathbf{q}}_k$ are components of the state \mathbf{x}_k .

Note that \mathbf{s}_l needs to be rotated with a proper rotation matrix R_k because the dipole magnitude that is encoded in $\bar{\mathbf{q}}_k$ should

not effect the term $R_k s_l$. Therefore, a normalization of the extended quaternion $\bar{\mathbf{q}}_k$ is required in that term.

A similar representation can also be used for the multi-object multi-dipole model (7) where $\mathbf{r}_{k,i}$ and $\bar{\mathbf{q}}_{k,i}$ then describe the position and the orientation of the i th object.

D. Discussion and Comparison

Three different orientation representations were proposed in this section:

- 1) A magnetic dipole vector $\mathbf{m}_k \in \mathbb{R}^3$ that encodes (i) two DoF for orientation and (ii) the magnitude of the magnetic dipole moment. This parametrization only works for single dipole objects, see Section III-A.
- 2) A unit quaternion $\mathbf{q}_k \in \mathbb{R}^4$ with $\|\mathbf{q}_k\| = 1$ that encodes three DoF for orientation. The magnitudes of the magnetic dipole moments are modeled with separate scalars $m_1, \dots, m_L \in \mathbb{R}$. This parametrization works for arbitrary multi-dipole objects, see Section III-B.
- 3) A (non-unit) quaternion $\bar{\mathbf{q}}_k \in \mathbb{R}^4$ that encodes (iii) three DoF for orientation and (iv) the common magnitude m of all magnetic dipole moments. This parametrization works for single dipole and multi-dipole objects where the relative magnitudes of the dipole moments are known, see Section III-C.

For the single dipole model (3), parametrization 1 is preferred because it only encodes the two DoF that are observable in that model. That model is also linear in \mathbf{m}_k , which is not the case if parametrization 2 or 3 would have been used. For the multi-dipole model (6), parametrization 2 or 3 are needed since all three DoF must be encoded.

In filtering applications that use unit quaternions for orientation representation, the quaternion needs to be normalized after each measurement update (often in an ad-hoc manner). If we use the third orientation representation, that normalization step can be omitted. This is because the norm of the quaternion contains information (the magnitude of the dipoles) that should be preserved. Therefore, if the relative magnitudes of the dipole moments are known, parametrization 3 is preferred since (i) no normalization step is required and (ii) less states are needed.

Finally, note that all three parametrizations have in common that they do not contain any singularities. In addition, \mathbf{m}_k , \mathbf{q}_k , and $\bar{\mathbf{q}}_k$ all have in common that their magnitudes should remain constant. This information is encoded in the motion models presented in Section V.

IV. ANALYSIS

The proposed possibility to use structures of dipoles opens up applications where full 6D tracking is possible. It is therefore important to understand the degree of observability of the sixth degree of freedom.

The observability of the single dipole model (3) has previously been discussed in [6] with the conclusion that at least two three-axis magnetometers are required to obtain observability for both the position and the two-dimensional orientation.

To analyze the observability of the multi-dipole model (6), we do a Taylor series expansion of the multi-dipole model (6) where we obtain

$$\sum_{l=1}^L J(\mathbf{r}_k + R_k \mathbf{s}_l) R_k \mathbf{b}_l \quad (14)$$

$$\approx \underbrace{J(\mathbf{r}_k) \mathbf{m}_k}_{(14a)} + \underbrace{\frac{3}{\|\mathbf{r}_k\|^5} \left(W_k - \left(\frac{5 \mathbf{r}_k^\top W_k \mathbf{r}_k}{2 \|\mathbf{r}_k\|^2} + \gamma \right) I \right) \mathbf{r}_k}_{(14b)},$$

where

$$\mathbf{m}_k = R_k \mathbf{b}, \quad W_k = R_k U R_k^\top, \quad (15a)$$

$$\mathbf{b} = \sum_{l=1}^L \mathbf{b}_l, \quad U = \sum_{l=1}^L \mathbf{s}_l \mathbf{b}_l^\top + \mathbf{b}_l \mathbf{s}_l^\top, \quad \gamma = \sum_{l=1}^L (\mathbf{b}_l^\top \mathbf{s}_l). \quad (15b)$$

The details are outlined in Appendix A. Based on this expansion, multiple properties of the multi-dipole model can be analyzed and explained.

The first term (14a) in the Taylor expansion is identical to the single dipole model (3), where the total dipole moment is the sum of all moments $\mathbf{m}_k = \sum_{l=1}^L \mathbf{m}_{k,l}$. On a distance far away from the object, this term dominates and the object appears as one single dipole. As for the single dipole model, only 2 DoF for the orientation are encoded in (14a). A rotation of the object around the magnetic dipole moment \mathbf{m}_k is not observable.

The orientation around \mathbf{m}_k is instead encoded in the higher order terms. Whereas the dipole term decays cubically $\|\mathbf{r}_k\|^{-3}$ with distance $\|\mathbf{r}_k\|$, the first higher order term (14b) decays to the power of four $\|\mathbf{r}_k\|^{-4}$. Therefore, the ability to estimate the orientation around \mathbf{m}_k decays faster with the distance $\|\mathbf{r}_k\|$ than the ability to estimate the remaining part of the orientation state.

Further, according to Appendix A, the second term (14a) remains unchanged for any additional 180° rotation around \mathbf{m}_k . Consequently, the last orientation state is not only more difficult to estimate, it is even more difficult to distinguish its true orientation from an orientation rotated 180°. This results in a bimodality of the corresponding likelihood. Higher order terms in the Taylor expansion may resolve this ambiguity, which has been found to be the case in our experiments. However, the information of this ambiguity decays to the power of five with distance.

As one particular illustration, Figure 2 shows the negative log likelihood (NLL)

$$-\log p(\mathbf{y}_k | \mathbf{x}_k) \propto 1/2 (\mathbf{y}_k - h(\mathbf{x}_k))^\top R^{-1} (\mathbf{y}_k - h(\mathbf{x}_k))$$

for a certain time instant k . The global minimum of the NLL is denoted with \mathbf{x}_k^* . Starting from that minimum, the angle β , corresponding to rotation around the vector \mathbf{m}_k , is adjusted and the NLL, $-\log p(\mathbf{y}_k | \mathbf{x}_k^*(\beta))$, is evaluated as a function of that angle. As a comparison, the same procedure is performed for the other two angles corresponding to rotations around the two axis orthogonal to \mathbf{m}_k .

As shown Figure 2, the likelihood exhibits a clear bimodality for the angle β , with two minima approximately 180° apart. This is in accordance with the theoretical analysis presented

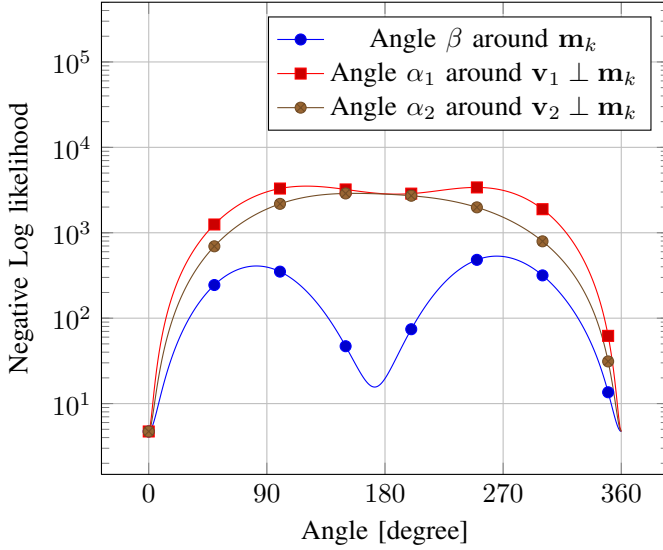


Fig. 2: Negative log likelihood (NLL) $-\log p(y_k | \mathbf{x}_k^*)$ as a function of the three angles β , α_1 and α_2 . The blue function marked with circles is the NLL as a function of the angle β around the magnetic dipole moment \mathbf{m}_k . The two angles α_1 and α_2 are rotations around the other two axis $\mathbf{v}_1, \mathbf{v}_2$ orthogonal to \mathbf{m}_k . The angles $\beta = 0$, $\alpha_1 = 0$, and $\alpha_2 = 0$ correspond to the global minimum of the NLL. From this global minimum, one angle is adjusted at a time.

above and in Appendix A. In addition, the variations of the NLL is smaller when β is varied compared to the other two angles α_1 and α_2 . This is also supported by the theoretical analysis in that rotation around β is harder to estimate than rotations around the other two axis orthogonal to \mathbf{m}_k .

V. MOTION MODEL

The motion model (1a) describes the dynamics of the state \mathbf{x}_k . It is described with a linear state-space model

$$\mathbf{x}_{k+1} = F_k \mathbf{x}_k + G_k \mathbf{w}_k, \quad \mathbf{w}_k \sim \mathcal{N}(\mathbf{0}, Q), \quad (16)$$

as commonly performed in target tracking applications. The state \mathbf{x}_k is divided into position state $\mathbf{x}_k^{\text{pos}}$ and orientation state $\mathbf{x}_k^{\text{ori}}$. The position state includes position and velocity $\mathbf{x}_k^{\text{pos}} = [\mathbf{r}_k^T, \mathbf{v}_k^T]^T$, whereas the orientation state includes orientation and angular velocity ω_k denoted by $\mathbf{x}_k^{\text{ori}} = [\mathbf{m}_k^T, \omega_k^T]^T$ or $\mathbf{x}_k^{\text{ori}} = [\mathbf{q}_k^T, \omega_k^T]^T$ depending on which of the two orientation representations that we use. The state-space is decomposed in a similar manner where

$$\mathbf{x}_k = \begin{bmatrix} \mathbf{x}_k^{\text{pos}} \\ \mathbf{x}_k^{\text{ori}} \end{bmatrix}, \quad F_k = \begin{bmatrix} F_k^{\text{pos}} & 0_3 \\ 0_3 & F_k^{\text{ori}} \end{bmatrix}, \quad G = \begin{bmatrix} G_k^{\text{pos}} & 0_3 \\ 0_3 & G_k^{\text{ori}} \end{bmatrix}, \quad (17)$$

$$Q = \begin{bmatrix} Q_k^{\text{pos}} & 0_3 \\ 0_3 & Q_k^{\text{ori}} \end{bmatrix}, \quad \mathbf{w}_k = \begin{bmatrix} \mathbf{w}_k^{\text{pos}} \\ \mathbf{w}_k^{\text{ori}} \end{bmatrix}.$$

We describe the motion model for \mathbf{x}^{pos} in Section V-A, and the motion model for the two representations of the orientation state in Section V-B and V-C. We use a constant velocity model for both position and orientation which is explained below.

A. Position State

To derive constant velocity motion model for the position, we model the velocity \mathbf{v} to be a Brownian motion. This can formally be written as

$$\frac{d}{dt} \mathbf{v}(t) = \mathbf{w}^{\text{pos}}(t), \quad (18)$$

where $\mathbf{w}(t)$ is white Gaussian noise.¹ Together with $\frac{d}{dt} \mathbf{r}(t) = \mathbf{v}(t)$ this gives the joint model

$$\frac{d}{dt} \begin{bmatrix} \mathbf{r}(t) \\ \mathbf{v}(t) \end{bmatrix} = \begin{bmatrix} 0_3 & I_3 \\ 0_3 & 0_3 \end{bmatrix} \begin{bmatrix} \mathbf{r}(t) \\ \mathbf{v}(t) \end{bmatrix} + \begin{bmatrix} 0_3 \\ I_3 \end{bmatrix} \mathbf{w}(t), \quad (19a)$$

$$\mathbb{E}[\mathbf{w}(t)\mathbf{w}(\tau)^T] = \sigma_{\text{pos}}^2 I_3 \delta(t - \tau), \quad (19b)$$

where $\mathbf{v}(t)$ is the velocity provided in global coordinates. This model can be derived from Newton's second law of motion, where the acceleration is interpreted as process noise, see for example [29] for more details. By following [28], we can derive a discrete-time constant velocity model for the position

$$\mathbf{x}_{k+1}^{\text{pos}} = F_k^{\text{pos}} \mathbf{x}_k^{\text{pos}} + G_k^{\text{pos}} \mathbf{w}_k^{\text{pos}}, \quad \mathbf{w}_k^{\text{pos}} \sim \mathcal{N}(\mathbf{0}, Q^{\text{pos}}), \quad (20)$$

where

$$F_k^{\text{pos}} = \begin{bmatrix} I_3 & TI_3 \\ 0_3 & I_3 \end{bmatrix}, \quad G_k^{\text{pos}} = \begin{bmatrix} TI_3 & 0_3 \\ 0_3 & I_3 \end{bmatrix}, \quad Q^{\text{pos}} = \frac{\sigma_{\text{pos}}^2}{T} \begin{bmatrix} \frac{1}{3}I_3 & \frac{1}{2}I_3 \\ \frac{1}{2}I_3 & I_3 \end{bmatrix}.$$

The derivation is also provided in, for example, [30].

B. Orientation State (Magnetic Dipole Moment)

In the first orientation representation (see Section III-A), the orientation is encoded by the magnetic dipole moment \mathbf{m} . To derive the motion model for \mathbf{m} , we consider its angular velocity ω provided in global coordinates. A vector \mathbf{m} that rotates around an axis $\omega/\|\omega\|$ with the angular speed $\|\omega\|$ obeys the following relation

$$\frac{d}{dt} \mathbf{m}(t) = \omega(t) \times \mathbf{m}(t) \quad (21a)$$

$$= -C(\omega(t))\mathbf{m}(t) = C(\mathbf{m}(t))\omega(t), \quad (21b)$$

where \times denotes the cross product and where

$$C(\mathbf{m}) = \begin{bmatrix} 0 & m_z & -m_y \\ -m_z & 0 & m_x \\ m_y & -m_x & 0 \end{bmatrix}. \quad (22)$$

In the same manner as in the previous section, we model the angular velocity ω to be a Brownian motion

$$\frac{d}{dt} \omega(t) = \mathbf{w}(t), \quad (23)$$

where $\mathbf{w}(t)$ is white Gaussian noise. This gives the joint model

$$\frac{d}{dt} \begin{bmatrix} \mathbf{m}(t) \\ \omega(t) \end{bmatrix} = \begin{bmatrix} 0_3 & C(\mathbf{m}(t)) \\ 0_3 & 0_3 \end{bmatrix} \begin{bmatrix} \mathbf{m}(t) \\ \omega(t) \end{bmatrix} + \begin{bmatrix} 0_3 \\ I_3 \end{bmatrix} \mathbf{w}(t), \quad (24a)$$

$$\mathbb{E}[\mathbf{w}(t)\mathbf{w}(\tau)^T] = \sigma_{\text{ori}}^2 \delta(t - \tau). \quad (24b)$$

¹Note that white continuous-time Gaussian noise does not exist in practice, for example, because it has infinite energy. However, we can still think of it as a \mathbf{w} as being driven by white noise. See [28] for further details.

We assume $C(\mathbf{m}(t))$ to be equal to $C(\mathbf{m}(t_k))$ in the interval $t \in [t_k, t_{k+1}]$. The discrete-time version of this constant velocity model for the orientation is then in the form

$$\mathbf{x}_{k+1}^{\text{ori}} = F_k^{\text{ori}} \mathbf{x}_k^{\text{ori}} + G_k^{\text{ori}} \mathbf{w}_k^{\text{ori}}, \quad \mathbf{w}_k^{\text{ori}} \sim \mathcal{N}(\mathbf{0}, Q^{\text{ori}}), \quad (25)$$

where

$$\begin{aligned} \mathbf{x}_k^{\text{ori}} &= \begin{bmatrix} \mathbf{m}_k \\ \boldsymbol{\omega}_k \end{bmatrix}, \quad F_k^{\text{ori}} = \begin{bmatrix} I_3 & TC(\mathbf{m}_k) \\ 0_3 & I_3 \end{bmatrix}, \\ G_k^{\text{ori}} &= \begin{bmatrix} T^2 C(\mathbf{m}_k) & 0_3 \\ 0_3 & TI_3 \end{bmatrix}, \quad Q^{\text{ori}} = \frac{\sigma_{\text{ori}}^2}{T} \begin{bmatrix} \frac{1}{3}I_3 & \frac{1}{2}I_3 \\ \frac{1}{2}I_3 & I_3 \end{bmatrix}. \end{aligned} \quad (26)$$

C. Orientation State (Quaternion)

In the second and third orientation representation (see Section III-B and III-C), the orientation is encoded by the unit quaternion \mathbf{q}_k and the extended quaternion $\bar{\mathbf{q}}_k$, respectively. The motion model for each of them is equivalent, so only $\bar{\mathbf{q}}_k$ is considered onwards. Its dynamics has a similar expression as in (21)

$$\frac{d}{dt} \bar{\mathbf{q}}(t) = \frac{1}{2} \boldsymbol{\omega}(t) \odot \bar{\mathbf{q}}(t) \quad (27a)$$

$$= \frac{1}{2} S(\boldsymbol{\omega}(t)) \bar{\mathbf{q}}(t) = \frac{1}{2} \bar{S}(\bar{\mathbf{q}}(t)) \boldsymbol{\omega}(t), \quad (27b)$$

where the cross product in (21) is replaced with the quaternion product \odot , and where $S(\boldsymbol{\omega})$ and $\bar{S}(\bar{\mathbf{q}})$ are defined as

$$S(\boldsymbol{\omega}) = \begin{bmatrix} 0 & -\omega_x & -\omega_y & -\omega_z \\ \omega_x & 0 & -\omega_z & \omega_y \\ \omega_y & \omega_z & 0 & -\omega_x \\ \omega_z & -\omega_y & \omega_x & 0 \end{bmatrix}, \quad \bar{S}(\bar{\mathbf{q}}) = \begin{bmatrix} -\bar{q}_1 & -\bar{q}_2 & -\bar{q}_3 \\ \bar{q}_0 & \bar{q}_3 & -\bar{q}_2 \\ -\bar{q}_3 & \bar{q}_0 & \bar{q}_1 \\ \bar{q}_2 & -\bar{q}_1 & \bar{q}_0 \end{bmatrix}.$$

As in (23), the angular velocity $\boldsymbol{\omega}$ is modeled to be driven by white Gaussian noise. This gives a similar expression of the joint model as in (24), where

$$\frac{d}{dt} \begin{bmatrix} \mathbf{q}(t) \\ \boldsymbol{\omega}(t) \end{bmatrix} = \begin{bmatrix} 0_{4 \times 4} & \frac{1}{2} \bar{S}(\bar{\mathbf{q}}(t)) \\ 0_{3 \times 4} & 0_{3 \times 3} \end{bmatrix} \begin{bmatrix} \bar{\mathbf{q}}(t) \\ \boldsymbol{\omega}(t) \end{bmatrix} + \begin{bmatrix} 0_{4 \times 3} \\ I_3 \end{bmatrix} \mathbf{w}(t), \quad (28a)$$

$$\mathbb{E}[\mathbf{w}(t) \mathbf{w}(\tau)^T] = \sigma_{\text{ori}}^2 I_3 \delta(t - \tau). \quad (28b)$$

By approximating $\bar{S}(\bar{\mathbf{q}}(t))$ to be equal to $\bar{S}(\bar{\mathbf{q}}(t_k))$ in the interval $t \in [t_k, t_{k+1}]$, we obtain a discrete-time model in the form (25), for which we have

$$\begin{aligned} \mathbf{x}_k^{\text{ori}} &= \begin{bmatrix} \bar{\mathbf{q}}_k \\ \boldsymbol{\omega}_k \end{bmatrix}, \quad F_k^{\text{ori}} = \begin{bmatrix} I_4 & \frac{T}{2} \bar{S}(\bar{\mathbf{q}}_k) \\ 0_{3 \times 4} & I_3 \end{bmatrix}, \\ G_k^{\text{ori}} &= \begin{bmatrix} \frac{T^2}{2} \bar{S}(\bar{\mathbf{q}}_k) & 0_{3 \times 4} \\ 0_{4 \times 3} & TI_3 \end{bmatrix}, \quad Q^{\text{ori}} = \frac{\sigma_{\text{ori}}^2}{T} \begin{bmatrix} \frac{1}{3}I_3 & \frac{1}{2}I_3 \\ \frac{1}{2}I_3 & I_3 \end{bmatrix}. \end{aligned} \quad (29)$$

D. Discussion

The motion models for the two orientation representations are in fact very similar. Essentially, the cross product in (21) is replaced with a quaternion product in (27a). It should also be noted that the angular velocity $\boldsymbol{\omega}$ in this section is provided in global coordinates. To obtain the dynamics of the angular velocity $\boldsymbol{\omega}$ in local coordinates, the quaternion multiplication in (27a) has to be swapped. However, a similar reformulation does not exist for the angular velocity in (21). This states an important difference between the two models.

E. Extended Kalman Filter

Based on the state-space model derived in the previous sections, the filtering problem can be solved using an extended Kalman filter (EKF). Given an initial state \mathbf{x}_0 and an initial state covariance P_0 , the filtering can be performed following Algorithm 1.

Algorithm 1 Extended Kalman filter with addition projection step

Initialize the estimate $\hat{\mathbf{x}}_{0|-1} = \mathbf{x}_0$ and $P_{0|-1} = P_0$.

for $k = 0$ to $N - 1$ **do**

1) Perform measurement update by computing

$$\hat{\mathbf{y}}_{k|k-1} = \mathbf{h}(\hat{\mathbf{x}}_{k|k-1}), \quad (30a)$$

$$H_k = \frac{d}{d\mathbf{x}_k} \mathbf{h}(\hat{\mathbf{x}}_{k|k-1}), \quad (30b)$$

$$S_k = H_k P_{k|k-1} H_k^T + R, \quad (30c)$$

$$K_k = P_{k|k-1} H_k^T S_k^{-1}, \quad (30d)$$

$$\hat{\mathbf{x}}_{k|k} = \hat{\mathbf{x}}_{k|k-1} + K_k (\mathbf{y}_k - \hat{\mathbf{y}}_{k|k-1}), \quad (30e)$$

$$P_{k|k} = (I - K_k H_k) P_{k|k-1}. \quad (30f)$$

2) Project the estimate onto the tracking volume

$$\hat{\mathbf{x}}_{k|k}^{\text{proj}} = \Pi_{\mathcal{C}}(\mathbf{x}_{k|k}). \quad (31)$$

Further, if $\mathbf{x}_{k|k} \notin \mathcal{C}$ then set the velocities $\mathbf{v}_{k|k} = \mathbf{0}$ and $\boldsymbol{\omega}_{k|k} = \mathbf{0}$ to zero

3) Perform time update by computing

$$\hat{\mathbf{x}}_{k+1|k} = F_k \hat{\mathbf{x}}_{k|k}^{\text{proj}}, \quad (32a)$$

$$P_{k+1|k} = F_k P_{k|k} F_k^T + Q_k. \quad (32b)$$

end for

If the estimated position $\hat{\mathbf{r}}_{k|k}$ is far away from the sensor network, both $\mathbf{h}(\hat{\mathbf{x}}_{k|k})$ and its derivative $\frac{d}{d\mathbf{x}_k} \mathbf{h}(\hat{\mathbf{x}}_{k|k})$ will be small. By following (30), this results in an uninformative measurement update $\mathbf{x}_{k|k} = \mathbf{x}_{k|k-1}$. This eventually leads to divergence of the filter. To prevent this, an additional projection step is included, see Step 2. This step is not included in the standard EKF, but makes this specific application more robust. By projected the filtered state $\mathbf{x}_{k|k}$ onto a set of the state-space in which the state should be contained under normal operation, this divergence can be prevented.

In this case, the set \mathcal{C} corresponds to a virtual box above the sensor network with the dimensions $1.2 \text{ m} \times 1.2 \text{ m} \times 0.6 \text{ m}$. Any estimated position $\hat{\mathbf{r}}_{k|k}$ that is outside this region is projected back onto this box. In addition, if any projection is needed, the velocities $\mathbf{v}_{k|k}$ and $\boldsymbol{\omega}_{k|k}$ are set to zero. We also consider a maximum value m_{max} of the magnetic dipole moment. This gives the restriction $\|\hat{\mathbf{m}}_{k|k}\| \leq m_{\text{max}}$ or $\|\hat{\mathbf{q}}_{k|k}\| \leq \sqrt{m_{\text{max}}}$ depending on which of the two orientation representations that are used.

VI. REAL DATA EXPERIMENTS

To validate the proposed models, real data experiments were conducted. A network that consists of four magnetometers (3-Axis Digital Compass IC, HMC5983, Honeywell) was

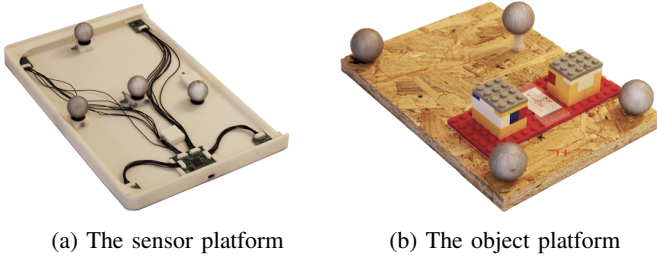


Fig. 3: The sensor and object platform with Vicon markers. The sensor platform has four three-axis magnetometers mounted in the corners of a rectangle. The object platform consist of two magnets (encapsulated in the two Lego blocks) aligned in orthogonal directions. That object platform was only used in the multi-dipole experiment. Photo: Martin Stenmark (2015).

designed with a sampling frequency of 220 Hz. The sensors were deployed in the corners of a rectangle with the dimension $30\text{ cm} \times 17.5\text{ cm}$. The sensor platform is shown in Figure 3a. With this sensor platform, experiments were conducted to validate both the single dipole model (3), and the multi-dipole model (6). To obtain ground truth data, an optical motion capture system (Vicon)² was used.

A. Single Dipole Experiment

The single dipole object consisted of two neodymium magnets mounted placed upon each other, both with a diameter of 12 mm and a height of 6 mm. Markers to be detected by the Vicon-system were attached to the object platform on which the magnets were attached, as well as to the sensor network.

During the experiments, the object platform was moved approximately 20 cm above the magnetometer network in different directions close to the magnetometer network.

For processing the data, the single dipole model (3) was used together with the two DoF orientation representation described in Section III-A. A constant velocity motion model was used for the position, see Section V-A, as well as for the orientation, see Section V-B. The process noise was set to $\sigma_{\text{pos}} = 0.1\text{ m s}^{-2}$ for the acceleration and $\sigma_{\text{ori}} = 1\text{ rad s}^{-2}$ for the angular acceleration. The covariance of the measurement noise was estimated using stationary data without any object.

In Figure 4a, all three Cartesian components of the estimated position are displayed together with the ground truth measured by the Vicon system. Note that the single dipole model is only able to estimate two DoF for orientation. These two DoF can be compared with the corresponding two DoF provided by the Vicon system. This is displayed in Figure 4b.

In all essence, both the full 3D position and 2D orientation are tracked with high accuracy. By comparing the estimated pose with the ground truth pose, the estimation performance for both the position and orientation can be computed.

²High accuracy reference measurements are provided through the use of the Vicon real-time tracking system courtesy of the UAS Technologies Lab, Artificial Intelligence and Integrated Computer Systems Division (AIICS) at the Department of Computer and Information Science (IDA), Linköping University, Sweden. <http://www.ida.liu.se/divisions/aiics/aiicssite/index.en.shtml>

TABLE I: Single dipole experiment: RMSE, bias and variance for position and orientation

Quantity	RMSE	Bias	$\sqrt{\text{Var}}$
Position	4.95 mm	4.90 mm	0.61 mm
Orientation	1.85°	1.82°	0.26°

In Table I, the performance is presented in terms of root-mean-square error (RMSE), which has been divided into variance and bias contribution; see Appendix B for how these quantities have been computed. The orientation error was computed according to (57a). According to that table, the sensor network can estimate position with a five millimeter accuracy in position and two of degrees accuracy in orientation. In these errors, the bias is clearly the dominating contribution.

B. Multi-Dipole Experiment

To acquire full position and orientation information, a multi-dipole object was constructed. Two neodymium magnets, each with a diameter of 12 mm and a height of 6 mm, were deployed perpendicularly on a distance 6.7 mm from each other, see Figure 1 for an illustration of this geometry. Figure 3b shows the object platform used in the experiment.

Three experiments were performed, each lasting approximately 100 s. For processing the data, the multi-dipole model was used, see Section II-B. Since the two magnets were of the same size, their magnitudes were assumed to be equal. Therefore, the extended quaternion $\bar{\mathbf{q}}_k$, see Section III-C, was used to model the orientation and the unknown magnitude together with the quaternion motion model presented in Section V-C. The same tuning parameters as in the single dipole experiment was used. For the first experiment, the results for both position and orientation are presented in Figure 5. Only a fraction of the time span is presented to make the plots readable. According to these plots, good tracking performance was achieved for all dimensions in both position and orientation. In Table II, the

TABLE II: Multiple dipole experiment: RMSE, bias and variance for position, full orientation and 2D orientation.

Quantity	RMSE	Bias	$\sqrt{\text{Var}}$
Position	11.89 mm	11.80 mm	1.14 mm
3D Orientation	8.80°	8.77°	0.58°
2D Orientation	4.97°	4.95°	0.37°

performance is computed in terms of RMSE, bias and variance in a similar manner as for Table I. The orientation error was computed according to (57b) in Appendix B. In comparison with the single dipole model, the estimation performance was twice as bad for position, and four times as bad for orientation in comparison with the single dipole experiment in Table I. The degraded performance is not surprising because an additional state is estimated in comparison to the previous model.

As discussed in Section IV, the NLL $-\log p(\mathbf{y}_k|\mathbf{x}_k)$ is less sensitive to rotations around the dipole moment \mathbf{m}_k than around any of the other two axis of rotation. This means

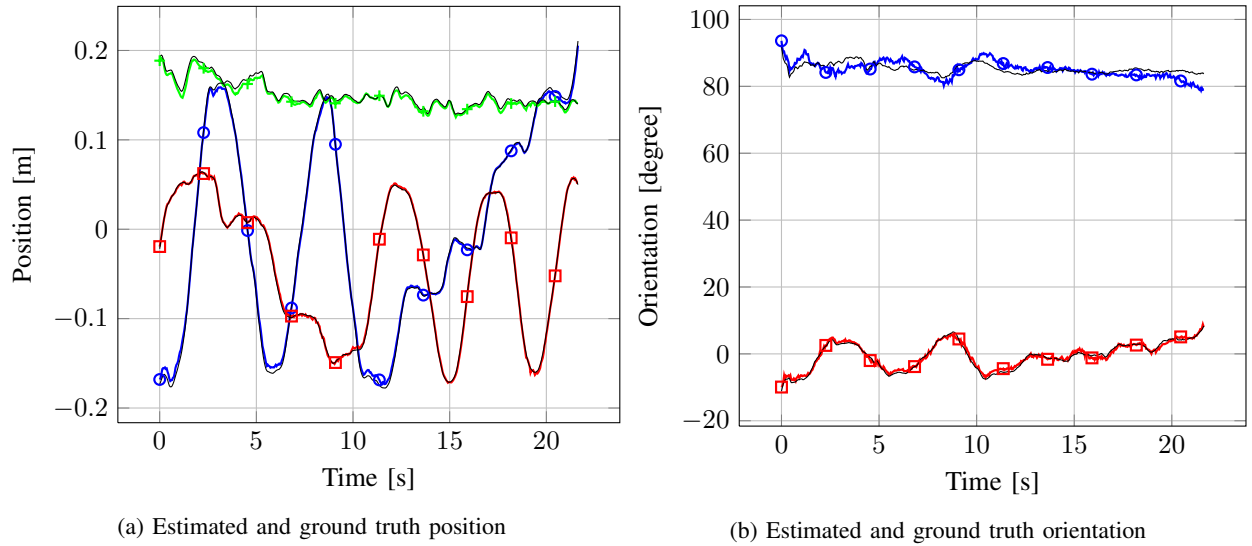


Fig. 4: Experiment with a single dipole object for tracking 5 DoF pose (3 DoF for position and 2 DoF for orientation). The estimates are displayed in colored, marked, thick line and the ground truth in thin unmarked black lines. Blue circle: x-coordinate/angle, red square: y-coordinate/angle, green cross: z-coordinate.

that the additional DoF for orientation, acquired by extending the single dipole model to a multi-dipole model, is harder to estimate than the remaining two DoF. To analyze this, the orientation error for the remaining two DoF are computed according to (57c). Both the 2D and the 3D orientation errors are presented in Table II and in Figure 6a. According to Table II, the 3D orientation error is almost twice as bad in comparison to the 2D orientation error.

A second experiment with the same experimental setup was also conducted. The orientation errors for that data set is presented in Figure 6b. As shown in that figure, the 2D orientation error is estimated correctly with a fairly low error (red curve). However, starting at time 40s, the full orientation error switches between the true and a false mode being approximately 180° apart. This can be addressed to the bimodal likelihood discussed in Section IV.

To circumvent this problem, a filter bank consisting of two EKFs was considered where each of them was restricted to be within each of the two modes. See for example [31, Chapter 10] for reference on Kalman filter banks. By evaluating the posterior of the two modes, the correct model could be selected. This strategy was tested on the same data set as displayed in Figure 6b and the result is presented in Figure 6c. According to that figure, the performance increases, however, the correct mode can still not always be resolved. A more reliable way to resolve this ambiguity is a subject for further research.

VII. APPLICATIONS

The magnetic localization technique described in this paper has multiple advantages in comparison to other localization techniques, for example, it (i) only includes low-cost components, (ii) does not require line-of-sight, and (iii) has a high accuracy in estimating both position and orientation. To show the applicability of the technique, four different demonstrators have been realized.

A. Virtual Watercolors

Museums and science centers have a high need for technology enabling interactive exhibits that encourage visitors to experiment and explore. In exhibits where spatial information is important, a localization system is required. These systems need to be intuitive for the visitors to control and interact with. In this context, the magnetic localization technique was used in an exhibition case mimicking water color painting, see Figure 7a. The user interacts using a regular painting brush equipped with a permanent magnet and the painting is displayed on a screen.

B. Interactive 3D Modeling

The hand-held device is also suitable for interaction and manipulation of three-dimensional virtual objects. The hand-held device equipped with a magnet can be used to pull, push and smoothen textures of an object, as well as moving and turning it, see Figure 7b. Both the virtual object and the virtual device can be observed through a head-mounted display making the interaction intuitive and realistic.

C. Digital Pathology

The magnetic localization technique has been used to improve the workstation that pathologists use when examining tissues. By mounting a magnet in a scalpel, see Figure 7c, a digital record can be constructed of the actions that have been performed. This saves time and also removes manual non-ergonomic activities.

D. Digital Table Hockey Game

By mounting a magnet in a puck for a table hockey game, the puck can be localized in real time, and meta information can be extracted, e.g., number of goals, see Figure 7d.

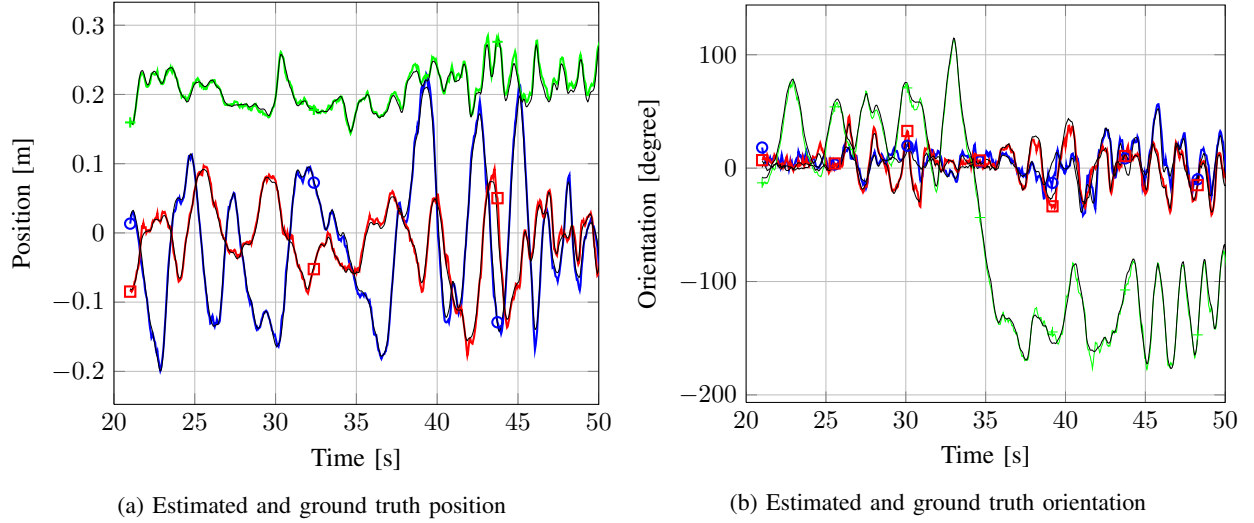


Fig. 5: Experiment with a multi-dipole object for tracking the full position and orientation state (3 DoF for position and 3 DoF for orientation). The estimates is displayed in colored, marked, thick line and the ground truth in thin unmarked black lines. Blue circle: x-coordinate/angle, red square: y-coordinate/angle, green cross: z-coordinate/angle.

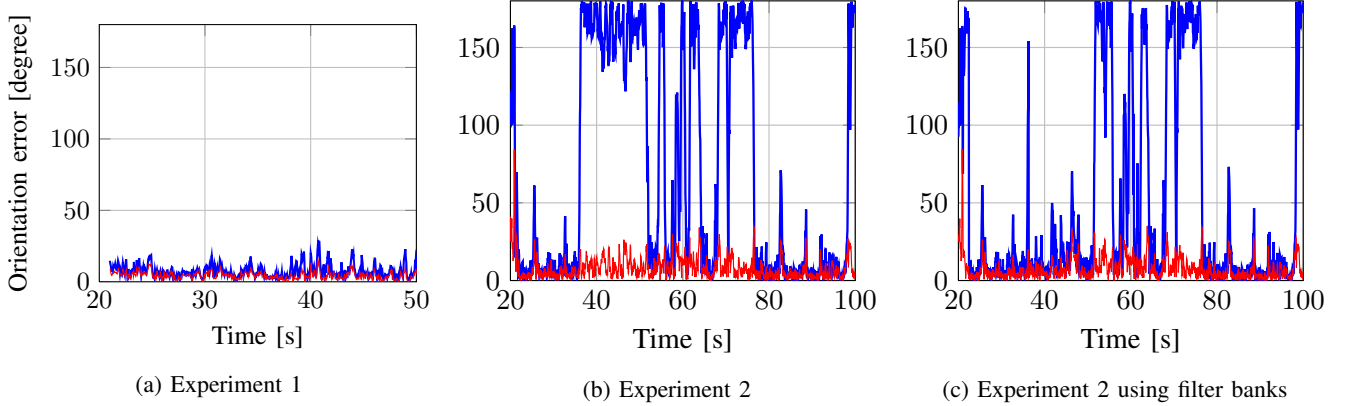


Fig. 6: Orientation error for experiment 1 and 2 with and without filter banks. Red: full 3D orientation error (57b), blue: 2D orientation error (57c).

VIII. CONCLUSION AND FUTURE WORK

In this paper, a framework for estimating the position and orientation of objects consisting of one or more magnetic dipoles was presented. The problem was cast into a statistical filtering problem, including both sensor models and motion models. The sensor models include (i) a point object model (one dipole), (ii) an extended object model (multi-dipole object) and (iii) multiple extended objects (multiple multi-dipole objects). Due to rotational symmetry, the point object model can only provide five degrees of freedom for position and orientation. Except for special geometries, this symmetry is not present in the extended object model, where all six degrees of freedom can be resolved. An analysis was provided showing that the sixth degree of freedom is weakly observable and bimodal. The models were validated on real data with a high-accuracy optical reference system. With a sensor network of four three-axis magnetometers, a tracking performance of 5 mm and 2° for model (i) and 12 mm and 9° for model (ii) was achieved. The vast majority of these errors consist of bias.

Future work should focus on dedicated calibration routines

for magnetometer networks. These routines may calibrate for position, orientation, bias, gain, and skewness of the magnetometers, as well as the parameters for the multi-dipole geometry. With a well calibrated sensor network, the bias contribution of the tracking performance could be significantly reduced. This would also facilitate resolving the ambiguity present in the multi-dipole object (ii).

APPENDIX A SUPPLEMENTARY DETAILS FOR SECTION IV

In this appendix, we investigate ambiguities for determining the orientation of the multi-dipole object. We consider the sensor model (6) in the form

$$\mathbf{f}(\varepsilon, R_k) = \sum_{l=1}^L J(\mathbf{r} + \varepsilon R_k \mathbf{s}_l) R_k \mathbf{b}_l, \quad (33)$$

where only one sensor (with position $\boldsymbol{\theta} = \mathbf{0}$) is considered to make the notation easier. In this appendix, the index $k = \{1, 2\}$ denotes two different instances of rotations that will

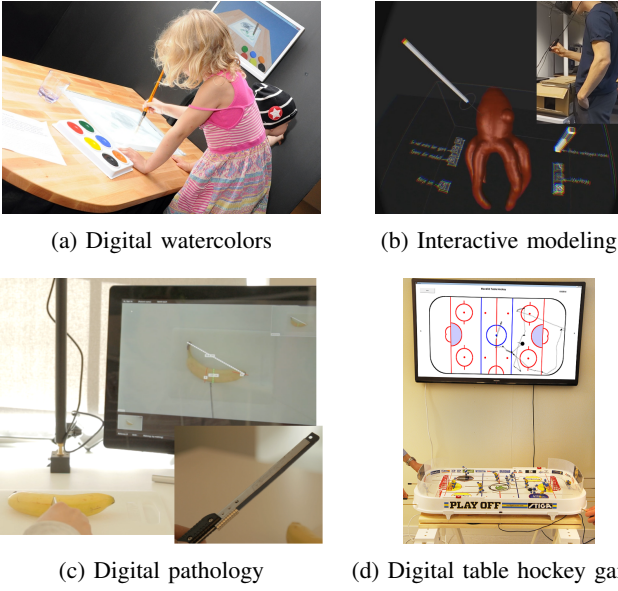


Fig. 7: Applications realized with the proposed technology. Photo: a) Anders Ynnerman (2012), b) Olle Grahn and Isabelle Forsman (2015), c) Linkin AB (2014), d) Martin Stenmarck (2015).

compared. Further, without loss of generality we also assume $\|\bar{\mathbf{q}}_k\| = 1$ and denote $R_k = R(\bar{\mathbf{q}}_k/\|\bar{\mathbf{q}}_k\|)$. The parameter ε determines the size of the multi-dipole object.

We want to analyze the properties of (33) when the object is far away from the sensor, or equivalently, if the object size is small, this means when $\varepsilon \rightarrow 0$. We perform this analysis with a Taylor expansion of (33) around $\varepsilon = 0$. By keeping the first two terms, we obtain

$$\mathbf{f}(\varepsilon, R_k) = \sum_{n=0}^{\infty} \frac{1}{n!} \frac{\partial^n}{\partial \varepsilon^n} \mathbf{f}(\varepsilon, R_k) \Big|_{\varepsilon=0} \varepsilon^n \quad (34a)$$

$$= \mathbf{f}(0, R_k) + \frac{\partial}{\partial \varepsilon} \mathbf{f}(\varepsilon, R_k) \Big|_{\varepsilon=0} \varepsilon + \mathcal{O}(\varepsilon^2) \quad (34b)$$

$$= \underbrace{A(R_k)}_{\text{1st term}} + \underbrace{B(R_k)}_{\text{2nd term}} \varepsilon + \mathcal{O}(\varepsilon^2). \quad (34c)$$

The term $A(R_k)$ decays as $\|\mathbf{r}\|^{-3}$ and $B(R)$ as $\|\mathbf{r}\|^{-4}$ with distance $\|\mathbf{r}\|$. Higher order terms decay as $\|\mathbf{r}\|^{-5}$ or more. Therefore, if the object is far away from the sensors, these two terms will dominate.

We introduce two rotation matrices R_1 and R_2 with

$$R_2 = \tilde{R}R_1, \quad (35)$$

where \tilde{R} is the rotation difference between R_1 and R_2 . We now derive conditions on the rotation difference \tilde{R} such that $A(R_1) = A(R_2)$ and $B(R_1) = B(R_2)$. More precisely, in the two following subsection we derive that

- 1) $A(R_1) = A(R_2)$ for all $\mathbf{r} \in \mathbb{R}^3$ when $\tilde{R}\mathbf{m}_1 = \mathbf{m}_1$, where $\mathbf{m}_1 = R_1 \sum_{l=1}^L \mathbf{b}_l$.
- 2) $A(R_1) = A(R_2)$ and $B(R_1) = B(R_2)$ for all $\mathbf{r} \in \mathbb{R}^3$ when $\tilde{R}\mathbf{m}_1 = \mathbf{m}_1$ and $\tilde{R}R = I$, i.e., a 180° rotation around \mathbf{m}_1 .

This means that any rotation 180° around \mathbf{m}_1 affects neither the first term, nor the second term in the Taylor expansion

(34). This results in a bimodal likelihood where the difference between these two modes only relies on even higher order terms in the Taylor expansion.

A. First Term $A(R_k)$

The first term in the Taylor expansion (34) is equal to the corresponding single dipole model

$$A(R_k) = \sum_{l=1}^L J(\mathbf{r}) R_k \mathbf{b}_l = J(\mathbf{r}) R_k \mathbf{b} = J(\mathbf{r}) \mathbf{m}_k, \quad (36)$$

where

$$\mathbf{m}_k = R_k \mathbf{b}, \quad \text{and} \quad \mathbf{b} = \sum_{l=1}^L \mathbf{b}_l. \quad (37)$$

As for the single dipole model, only two out of three DoF for orientation are observable. We perform this analysis by considering the difference $A(R_2) - A(R_1)$. If this expression is zero for some certain choice of rotation difference \tilde{R} , the two orientations R_1 and R_2 cannot be resolved based on this term.

Theorem 1: Consider the single dipole term (36). Then

$$A(R_1) = A(R_2) \quad \forall \mathbf{r} \in \mathbb{R}^3 \quad (38a)$$

if and only if

$$\tilde{R}\mathbf{m}_1 = \mathbf{m}_1, \quad \text{where} \quad \mathbf{m}_1 = R_1 \sum_{l=1}^L \mathbf{b}_l \quad (38b)$$

and where \tilde{R} is given by (35).

Proof: Consider

$$A(R_2) - A(R_1) = J(\mathbf{r}) \tilde{R}R_1 \mathbf{b} - J(\mathbf{r}) R_1 \mathbf{b} \quad (39)$$

$$= J(\mathbf{r}) (\tilde{R}\mathbf{m}_1 - \mathbf{m}_1), \quad (40)$$

which is equal to zero for all \mathbf{r} if and only if

$$\tilde{R}\mathbf{m}_1 = \mathbf{m}_1. \quad (41)$$

Consequently, if the object is far away from the sensor, the dipole term will dominate and the third DoF for the orientation (the one that corresponds to rotation around \mathbf{m}_1) will be the hardest one to estimate. ■

B. Second Term $B(R_k)$

The second term of the Taylor expansion (34) can be expressed as

$$\begin{aligned}
 B(R_k) &= \sum_{l=1}^L \frac{\partial J(\mathbf{r}) R_k \mathbf{b}_l}{\partial \mathbf{r}} R_k \mathbf{s}_l \\
 &= \sum_{l=1}^L \frac{3}{\|\mathbf{r}\|^5} \left((\mathbf{b}_l^\top R_k^\top \mathbf{r}) I + \mathbf{r} \mathbf{b}_l^\top R_k^\top + R_k \mathbf{b}_l \mathbf{r}^\top \right. \\
 &\quad \left. - 5 \frac{\mathbf{r} \mathbf{r}^\top}{\mathbf{r}^\top \mathbf{r}} (\mathbf{b}_l^\top R_k^\top \mathbf{r}) \right) R_k \mathbf{s}_l \\
 &= \sum_{l=1}^L \frac{3}{\|\mathbf{r}\|^5} \left(R_k \mathbf{s}_l \mathbf{b}_l^\top R_k^\top + (\mathbf{b}_l^\top \mathbf{s}_l) I + R_k \mathbf{b}_l \mathbf{s}_l^\top R_k^\top \right. \\
 &\quad \left. - \frac{5 \mathbf{r}^\top (R_k \mathbf{s}_l \mathbf{b}_l^\top R_k^\top + R_k \mathbf{b}_l \mathbf{s}_l^\top R_k^\top) \mathbf{r}}{2 \|\mathbf{r}\|^2} I \right) \mathbf{r} \\
 &= \frac{3}{\|\mathbf{r}\|^5} \left(W_k - \frac{5 \mathbf{r}^\top W_k \mathbf{r}}{2 \|\mathbf{r}\|^2} I + \sum_{l=1}^L (\mathbf{b}_l^\top \mathbf{s}_l) I \right) \mathbf{r}, \quad (42)
 \end{aligned}$$

where

$$W_k = R_k U R_k^\top, \quad \text{with} \quad U = \sum_{l=1}^L \mathbf{s}_l \mathbf{b}_l^\top + \mathbf{b}_l \mathbf{s}_l^\top. \quad (43)$$

We want to analyze under which conditions $B(R_2) = B(R_1)$. The analysis is performed in the same manner as for the single dipole term by considering the difference

$$\begin{aligned}
 B(R_2) - B(R_1) &= \frac{3}{\|\mathbf{r}\|^5} \left((\tilde{R} W_1 \tilde{R}^\top - W_1) - \frac{5 \mathbf{r}^\top (\tilde{R} W_1 \tilde{R}^\top - W_1) \mathbf{r}}{2 \|\mathbf{r}\|^2} I \right) \mathbf{r}. \quad (44)
 \end{aligned}$$

One can easily conclude that (44) is equal to zero for all $\mathbf{r} \in \mathbb{R}^3$ if and only if

$$\tilde{R} W_1 \tilde{R}^\top - W_1 = 0. \quad (45)$$

Before deriving the condition on W_1 and \tilde{R} for this equality to hold, the center of the object needs to be defined.

The position of each dipole is described (in local coordinates) as a displacement \mathbf{s}_l relative to the center of the object. Obviously, this center is not unique. We assume the center of the object has been selected such that

$$\underbrace{\left(\sum_{l=1}^L \mathbf{s}_l \mathbf{b}_l^\top + \mathbf{b}_l \mathbf{s}_l^\top \right)}_{=U} \underbrace{\sum_{l=1}^L \mathbf{b}_l}_{=\mathbf{b}} = \mathbf{0}. \quad (46)$$

If this property does not hold for the selected center of the object, a new center can be defined using the following translation

$$\mathbf{s}_l^{\text{new}} = \mathbf{s}_l - \Delta \mathbf{s}, \quad \text{where} \quad (47a)$$

$$\Delta \mathbf{s} = \frac{1}{\mathbf{b}^\top \mathbf{b}} \left(I - \frac{\mathbf{b} \mathbf{b}^\top}{2 \mathbf{b}^\top \mathbf{b}} \right) U \mathbf{b}. \quad (47b)$$

By using $\mathbf{s}_l^{\text{new}}$ in (46), that property is indeed fulfilled. Note that W_k has also an eigenvalue 0 with the eigenvector \mathbf{m}_k

since $W_k \mathbf{m}_k = R_k U R_k^\top \mathbf{m}_k = R_k U \mathbf{b} = \mathbf{0}$. With this definition of the center of the object, the following theorem provides the condition for (44) to be equal to zero.

Lemma 1: Consider a symmetric matrix $W = W^\top \in \mathbb{R}^{3 \times 3}$ and a rotation matrix $\tilde{R} \in \text{SO}(3)$. Also assume that they have a common eigenvector \mathbf{m} with

$$W \mathbf{m} = \mathbf{0}, \quad \tilde{R} \mathbf{m} = \mathbf{m}. \quad (48a)$$

Then

$$\tilde{R} W \tilde{R}^\top - W = 0 \quad (48b)$$

if and only if $\tilde{R} \tilde{R} = I$ or $\lambda_1 = \lambda_2$, where λ_1 and λ_2 are the two non-zero eigenvalues of W .

Proof: Since W is symmetric, it can be written

$$W = Q D Q^\top, \quad (49)$$

where Q is orthogonal and $\det(Q) = 1$. Since $W \mathbf{m} = \mathbf{0}$, one of the diagonal components in D is zero. We can without loss of generality order the eigenvalues such that $D = \text{diag}(\lambda_1, \lambda_2, 0)$. Since both W and \tilde{R} share the same eigenvector \mathbf{m} with eigenvalue 0 and 1, respectively, we have that

$$Q^\top W Q = \begin{bmatrix} \lambda_1 & 0 & 0 \\ 0 & \lambda_2 & 0 \\ 0 & 0 & 0 \end{bmatrix}, \quad Q^\top \tilde{R} Q = \begin{bmatrix} c(\theta) & -s(\theta) & 0 \\ s(\theta) & c(\theta) & 0 \\ 0 & 0 & 1 \end{bmatrix},$$

where θ corresponds to the rotation angle around \mathbf{m} and $c(\theta) = \cos(\theta)$, $s(\theta) = \sin(\theta)$. By applying Q^\top from the left and Q from the right on (48b), we obtain

$$\begin{aligned}
 Q^\top \tilde{R} W \tilde{R}^\top Q - Q^\top W Q &= Q^\top \tilde{R} Q D Q^\top \tilde{R}^\top Q - D \\
 &= \begin{bmatrix} c(\theta) & -s(\theta) & 0 \\ s(\theta) & c(\theta) & 0 \\ 0 & 0 & 1 \end{bmatrix} \begin{bmatrix} \lambda_1 & 0 & 0 \\ 0 & \lambda_2 & 0 \\ 0 & 0 & 0 \end{bmatrix} \begin{bmatrix} c(\theta) & s(\theta) & 0 \\ -s(\theta) & c(\theta) & 0 \\ 0 & 0 & 1 \end{bmatrix} - \begin{bmatrix} \lambda_1 & 0 & 0 \\ 0 & \lambda_2 & 0 \\ 0 & 0 & 0 \end{bmatrix} \\
 &= (\lambda_1 - \lambda_2) s(\theta) \begin{bmatrix} -s(\theta) & c(\theta) & 0 \\ c(\theta) & s(\theta) & 0 \\ 0 & 0 & 0 \end{bmatrix}. \quad (50)
 \end{aligned}$$

This expression is equal to zero if and only if $\lambda_1 = \lambda_2$ or $\theta = n\pi$, where $n \in \mathbb{Z}$, which implies that $\tilde{R} = \tilde{R}^\top$. ■

The conclusion is now formalized in the following theorem.

Theorem 2: Consider the single dipole term (36) and the higher order term (42). Further, assume that the center of the object has been defined such that (46) is fulfilled. Then

$$A(R_1) = A(R_2) \quad \text{and} \quad B(R_1) = B(R_2) \quad \forall \mathbf{r} \in \mathbb{R}^3 \quad (51)$$

if and only if

$$\tilde{R} \mathbf{m}_1 = \mathbf{m}_1 \quad \text{and} \quad \tilde{R} = \tilde{R}^\top, \quad (52)$$

or

$$\tilde{R} \mathbf{m}_1 = \mathbf{m}_1 \quad \text{and} \quad \lambda_1 = \lambda_2, \quad (53)$$

where $\mathbf{m}_1 = R_1 \sum_{l=1}^L \mathbf{b}_l$ is given by (37), \tilde{R} is given by (35), and λ_1 and λ_2 are eigenvalues of U defined in (43).

Proof: From Lemma 1, we know that $A(R_1) = A(R_2) \quad \forall \mathbf{r} \in \mathbb{R}^3$ is fulfilled if and only if $\tilde{R} \mathbf{m}_1 = \mathbf{m}_1$. For the second equality, we have

$$B(R_2) - B(R_1) = \frac{3}{\|\mathbf{r}\|^5} \left(V - \frac{5 \mathbf{r}^\top V \mathbf{r}}{2 \|\mathbf{r}\|^2} I \right) \mathbf{r}, \quad (54)$$

with

$$V = \tilde{R}W_1\tilde{R}^T - W_1, \quad (55)$$

where W_1 is given by (43). Further, since $U\mathbf{b} = \mathbf{0}$, we have that $W_1\mathbf{m}_1 = R_1UR_1^T\mathbf{m}_1 = R_1U\mathbf{b} = \mathbf{0}$. According to Lemma 1, equation (55) is fulfilled if and only if $\tilde{R}\tilde{R} = I$ or $\lambda_1 = \lambda_2$, where λ_1 and λ_2 are the two non-zero eigenvalues of W_1 . Finally we notice that $W_1 = R_1UR_1^T$ has the same eigenvalues as U , since R_1 is orthogonal. Consequently, λ_1 and λ_2 are also eigenvalues of U . This completes the proof. ■

Remark 1: The condition $\lambda_1 = \lambda_2$ provides a condition on the dipole geometry encoded in U (43). The geometry should consequently not be chosen such that $\lambda_1 = \lambda_2$. Instead, it should preferably be chosen such that these two eigenvalues are as separated as possible.

APPENDIX B PERFORMANCE MEASURES

This appendix gives details about the performance measure that was used in the result section.

With the estimated position $\hat{\mathbf{r}}_k$ and the ground truth position \mathbf{r}_k^0 , the estimation error was computed as

$$\boldsymbol{\epsilon}_k^{\text{pos}} = \hat{\mathbf{r}}_k - \mathbf{r}_k^0. \quad (56)$$

The orientation error was computed differently depending on the sensor model. For the single dipole model (3), the orientation error was computed as the angle between the true and estimated direction of the dipole moment

$$\boldsymbol{\epsilon}_k^{\text{ori}} = \arccos \left(\frac{\hat{\mathbf{m}}_{k|k}^T R(\mathbf{q}_k^0) \mathbf{b}}{\|\hat{\mathbf{m}}_{k|k}\| \|\mathbf{b}\|} \right), \quad (57a)$$

where \mathbf{q}_k^0 is the quaternion describing the true orientation. This orientation error was used in Section VI-A.

For the multi-dipole model, the full orientation error was computed as the shortest angle between the estimated and true quaternion as

$$\boldsymbol{\epsilon}_k^{\text{ori,3D}} = 2 \arccos \left(\frac{|\hat{\mathbf{q}}_{k|k}^T \mathbf{q}_k^0|}{\|\hat{\mathbf{q}}_{k|k}\| \|\mathbf{q}_k^0\|} \right). \quad (57b)$$

For the multi-dipole model, the 2D orientation error was computed in the same manner as for the single dipole case as the angle between the true and estimated direction of the dipole moment vector

$$\boldsymbol{\epsilon}_k^{\text{ori,2D}} = \arccos \left(\left(R \left(\frac{\hat{\mathbf{q}}_{k|k}}{\|\hat{\mathbf{q}}_{k|k}\|} \right) \mathbf{b} \right)^T R(\mathbf{q}_k^0) \mathbf{b} \right). \quad (57c)$$

The error (57b) and (57c) were used in Section VI-B.

For each of these errors, the corresponding root-mean-square error was computed as

$$\text{RMSE} = \sqrt{\frac{1}{N} \sum_{k=1}^N \|\boldsymbol{\epsilon}_k\|^2}. \quad (58)$$

This quantity can be decomposed in a bias and a variance part. A 4th order Butterworth-filter with the cutoff frequency

$f_c = 10 \text{ Hz}$ was used to separate the error in a low and high frequency part

$$\boldsymbol{\epsilon}_k = \boldsymbol{\epsilon}_k^{\text{low}} + \boldsymbol{\epsilon}_k^{\text{high}} \quad (59)$$

and the variance and bias contributions to RMSE can be defined as

$$\sqrt{\text{variance}} = \sqrt{\frac{1}{N} \sum_{k=1}^N \frac{1}{1 - 2Tf_c} \|\boldsymbol{\epsilon}_k^{\text{high}}\|^2}, \quad (60a)$$

$$\text{bias} = \sqrt{\frac{1}{N} \sum_{k=1}^N \|\boldsymbol{\epsilon}_k\|^2 - \frac{1}{1 - 2Tf_c} \|\boldsymbol{\epsilon}_k^{\text{high}}\|^2}. \quad (60b)$$

REFERENCES

- [1] E. Stathopoulos, V. Schlageter, B. Meyrat, Y. Ribaupierre, and P. Kucera, "Magnetic pill tracking: a novel non-invasive tool for investigation of human digestive motility," *Neurogastroenterology & Motility*, vol. 17, no. 1, pp. 148–154, 2005.
- [2] R. Guignet, G. Bergonzelli, V. Schlageter, M. Turini, and P. Kucera, "Magnet Tracking: a new tool for in vivo studies of the rat gastrointestinal motility," *Neurogastroenterology & Motility*, vol. 18, no. 6, pp. 472–478, 2006.
- [3] X. Wang, M.-H. Meng, and C. Hu, "A localization method using 3-axis magnetoresistive sensors for tracking of capsule endoscope," in *Proceedings of the 8th Annual International Conference of the IEEE Engineering in Medicine and Biology Society (EMBS)*, New York, NY, USA, Aug. 2006, pp. 2522–2525.
- [4] M. Birsan, "Unscented particle filter for tracking a magnetic dipole target," in *Proceedings of MTS/IEEE OCEANS*, Washington, DC, USA, Sep. 2005.
- [5] R. J. Kozick and B. M. Sadler, "Joint processing of vector-magnetic and acoustic-sensor data," in *SPIE Unattended Ground, Sea, and Air Sensor Technologies and Applications IX*, vol. 6562, 2007.
- [6] N. Wahlström and F. Gustafsson, "Magnetometer modeling and validation for tracking metallic targets," *IEEE Transactions on Signal Processing*, vol. 62, no. 3, pp. 545–556, 2014.
- [7] C. Harrison and S. E. Hudson, "Abracadabra: Wireless, high-precision, and unpowered finger input for very small mobile devices," in *Proceedings of the 22nd Annual ACM Symposium on User Interface Software and Technology (UIST)*, Victoria, BC, Canada, Oct. 2009, pp. 121–124.
- [8] D. Ashbrook, P. Baudisch, and S. White, "Nenya: Subtle and eyes-free mobile input with a magnetically-tracked finger ring," in *Proceedings of the SIGCHI Conference on Human Factors in Computing Systems (CHI)*, Vancouver, BC, Canada, May 2011, pp. 2043–2046.
- [9] L. Chan, R.-H. Liang, M.-C. Tsai, K.-Y. Cheng, C.-H. Su, M. Y. Chen, W.-H. Cheng, and B.-Y. Chen, "Fingerpad: Private and subtle interaction using fingertips," in *Proceedings of the 26th Annual ACM Symposium on User Interface Software and Technology (UIST)*, St Andrews, UK, Oct. 2013, pp. 255–260.
- [10] R.-H. Liang, K.-Y. Cheng, C.-H. Su, C.-T. Weng, B.-Y. Chen, and D.-N. Yang, "Gaussense: Attachable stylus sensing using magnetic sensor grid," in *Proceedings of the 25th Annual ACM Symposium on User Interface Software and Technology (UIST)*, Cambridge, MA, USA, Oct. 2012, pp. 319–326.
- [11] D. R. Haynor, C. P. Somogyi, R. N. Golden, and G. B. Sanders, "System and method to determine the location and orientation of an indwelling medical device," Jul. 17 2001, US Patent 6,263,230.
- [12] W. A. Beck, "Localization of small magnets against a noisy background," in *Saratov Fall Meeting 2000*. Saratov, Russia: International Society for Optics and Photonics, 2001, pp. 6–12.
- [13] S. Yabukami, H. Kikuchi, M. Yamaguchi, K. Arai, K. Takahashi, A. Itagaki, and N. Wako, "Motion capture system of magnetic markers using three-axial magnetic field sensor," *IEEE Transactions on Magnetics*, vol. 36, no. 5, pp. 3646–3648, 2000.
- [14] V. Schlageter, P.-A. Besse, R. Popovic, and P. Kucera, "Tracking system with five degrees of freedom using a 2D-array of hall sensors and a permanent magnet," *Sensors and Actuators A: Physical*, vol. 92, no. 1, pp. 37–42, 2001.
- [15] S. Yabukami, H. Kanetaka, N. Tsuji, A. Itagaki, M. Yamaguchi, K. Arai, and H. Mitani, "A new tracking system of jaw movement using two magnets," *IEEE Transactions on Magnetics*, vol. 38, no. 5, pp. 3315–3317, 2002.

- [16] S. Yabukami, K. Arai, K. Arai, and S. Tsuji, "Magnetic wireless motion capturing system and its application for jaw tracking system and 3D computer input device," *Journal of Magnetism*, vol. 8, no. 1, pp. 70–73, 2003.
- [17] C. Hu, M. Q.-H. Meng, and M. Mandal, "Efficient magnetic localization and orientation technique for capsule endoscopy," *International Journal of Information Acquisition*, vol. 2, no. 1, pp. 23–36, 2005.
- [18] C. Hu, M.-H. Meng, M. Mandal, and X. Wang, "3-axis magnetic sensor array system for tracking magnet's position and orientation," in *Proceedings of the 6th World Congress on Intelligent Control and Automation (WCICA)*, vol. 2. Dalian, China: IEEE, 2006, pp. 5304–5308.
- [19] C. Hu, W. Yang, D. Chen, M.-H. Meng, and H. Dai, "An improved magnetic localization and orientation algorithm for wireless capsule endoscope," in *Proceedings of the 30th Annual International Conference of the IEEE Engineering in Medicine and Biology Society (EMBS)*, Vancouver, BC, Canada, Aug. 2008, pp. 2055–2058.
- [20] C. Hu, M. Li, S. Song, R. Zhang, M.-H. Meng *et al.*, "A cubic 3-axis magnetic sensor array for wirelessly tracking magnet position and orientation," *IEEE Sensors Journal*, vol. 10, no. 5, pp. 903–913, 2010.
- [21] J. T. Sherman, J. K. Lubkert, R. S. Popovic, and M. R. DiSilvestro, "Characterization of a novel magnetic tracking system," *IEEE Transactions on Magnetism*, vol. 43, no. 6, pp. 2725–2727, 2007.
- [22] M. Birsan, "Non-linear Kalman filters for tracking a magnetic dipole," in *Proceedings of the International Conference on Marine Electromagnetics*, London, UK, Mar. 2004.
- [23] R. J. Kozick and B. M. Sadler, "Classification via information-theoretic fusion of vector-magnetic and acoustic sensor data," in *Proceedings of International Conference on Acoustics, Speech and Signal Processing (ICASSP)*, vol. 2, Honolulu, HI, USA, Apr. 2007, pp. 953–956.
- [24] —, "Algorithms for tracking with an array of magnetic sensors," in *Sensor Array and Multichannel Signal Processing Workshop (SAM)*, Darmstadt, Germany, Jul. 2008, pp. 423–427.
- [25] W. Koch, "Bayesian approach to extended object and cluster tracking using random matrices," *IEEE Transactions on Aerospace and Electronic Systems*, vol. 44, no. 3, pp. 1042–1059, Jul. 2008.
- [26] N. A. Chaturvedi, A. K. Sanyal, and N. H. McClamroch, "Rigid-body attitude control," *IEEE Control Systems*, vol. 31, no. 3, pp. 30–51, 2011.
- [27] J. B. Kuipers, *Quaternions and rotation sequences*. Princeton, NJ, USA: Princeton university press, 1999.
- [28] A. H. Jazwinski, *Stochastic Processes and Filtering Theory*, ser. Mathematics in Science and Engineering. New York, NY, USA: Academic Press, 1970, vol. 64.
- [29] X. R. Li and V. P. Jilkov, "Survey of maneuvering target tracking. part i. dynamic models," *IEEE Transactions on Aerospace and Electronic Systems*, vol. 39, no. 4, pp. 1333–1364, 2003.
- [30] M. S. Grewal and A. P. Andrews, *Kalman Filtering. Theory and Practice Using MATLAB*, 3rd ed. Hoboken, NJ, USA: John Wiley & Sons, 2008.
- [31] F. Gustafsson, *Statistical Sensor Fusion*, 1st ed. Studentlitteratur, 2012, page 257-272.